# Utilizing Ultraviolet Photons to Generate Single Photon Emitters in Semiconductor Monolayers

Wei Wang, <sup>1,2</sup> Leighton O. Jones, <sup>3</sup> Jia-Shiang Chen, <sup>1,4</sup> George C. Schatz, <sup>3,4</sup> Xuedan Ma<sup>1,2,4\*</sup>

<sup>1</sup>Center for Nanoscale Materials, Argonne National Laboratory, Lemont, IL 60439, USA

<sup>2</sup>Consortium for Advanced Science and Engineering, University of Chicago, Chicago, Illinois 60637, United States

<sup>3</sup>Department of Chemistry, Northwestern University, Evanston, Illinois 60208, United States

<sup>4</sup>Center for Molecular Quantum Transduction, Northwestern-Argonne Institute of Science and Engineering, Northwestern University, Evanston, IL 60208, USA

## **ABSTRACT**

The understanding and controlled creation of atomic defects in semiconductor transition metal dichalcogenides (TMDs) are highly relevant to their applications in high performance quantum optics and nanoelectronic devices. Here, we demonstrate a versatile approach in generating single photon emitters in MoS<sub>2</sub> monolayers using widely attainable UV light. We discover that only defects engendered by UV photons in vacuum exhibit single photon emitter characteristics, whereas those created in air lack quantum emission attributes. In combination with theoretical calculations, we assign the defects generated in vacuum to unpassivated sulfur vacancies, whose highly localized mid-gap states give rise to single photon emission. In contrast, UV irradiation of

the MoS<sub>2</sub> monolayers in air results in oxygen-passivated sulfur vacancies, whose optical properties are likely governed by their pristine band-to-defect band optical transitions. These findings suggest that widely available light sources such as UV light can be utilized for creating quantum photon sources in TMDs.

KEYWORDS: transition metal dichalcogenides, single photon emitter, quantum defect, sulfurvacancy, UV irradiation, oxygen-passivated defect

### INTRODUCATION

The field of semiconductor science is intimately intertwined with defect physics. The device application of a bulk semiconductor relies closely on the understanding and precise control of its intrinsic defects, which are often deemed detrimental to device performance. On the other hand, defects have been used for deliberate functionalization of semiconductors, particularly in their low dimensional structures. Defects with tailored electronic structures in two-dimensional transition metal dichalcogenides (TMDs) have been used for nonvolatile memristors, efficient photon upconversion, and high performance catalysis. Among the various opportunities enabled by defect engineering, the controlled creation of quantum photon sources in TMDs has attracted considerable interest, primarily because the particular characteristics of the TMDs such as their large exciton binding energies and natural suitability for device integration  $^{11, 12}$  render them prime host materials for large-scale quantum photon source arrays. Valley pseudospins in TMDs due to the confinement of charge carriers at the  $\pm K$  valleys  $^{13, 14}$  and high quality mechanical

resonances owing to their ultralow mass<sup>15, 16</sup> lend additional degree of freedom for interfacing photonics with valleytronics and optomechanics.

Quantum defects in TMDs that support single photon emission can be intentionally introduced via local strain modification. 17-20 While this approach is viable for the scalable creation of quantum defects in TMD monolayers, 17-19 it offers limited spatial precision and requires auxiliary mechanisms to induce local strains. 21 Focused ion beam irradiation, in which ion-beams with landing energies on orders of tens to hundreds of keV are used to bombard TMD monolayers, provide an alternative approach for creating quantum defects with high spatial precision. 21-23 However, the scalability of this method can be hindered due to the requirement of complex instrumentation. Progressing from these achievements, a scalable approach that allows the generation of quantum photon sources in TMDs with high spatial precision while utilizing easily accessible laboratory instruments is highly desirable.

Indeed, recent advances in the understanding of defect structures allude the possibility of an entirely different avenue for creating quantum photon sources in TMDs. Specifically, single photon emitters (SPEs) in TMDs have been discovered to be primarily associated with chalcogen vacancies, <sup>24, 25</sup> the formation energies of which are merely a few eV, much smaller than those of the corresponding transition metal vacancies in these materials. <sup>24, 26, 27</sup> As such, activation energies provided by in-vacuo high temperature annealing are sufficient for creating sulfur vacancies in MoS<sub>2</sub> monolayers. <sup>22, 25</sup> It is therefore conceivable, and alluring at the same time, to create such quantum defects by leveraging nowadays mature lighting technologies that afford ample options for generating electromagnetic waves with precisely controlled photon energies, powers and profiles. <sup>28, 29</sup> Yet it remains to be answered if photon energies are sufficient for creating relevant

quantum defects suitable for single photon emission, and the associated conditions that are necessary for their controlled generation.

Driven by these open questions and the quest for more versatile SPE generation approaches, in this study, we explore the viability of creating SPEs in TMDs using widely available light sources. We apply high energy photons, namely UV light, to irradiate MoS<sub>2</sub> monolayers and demonstrate the formation of quantum defects capable of single photon emission. We find the success of this approach relies critically on the irradiation environment: only defects that are engendered in vacuum exhibit SPE characteristics, whereas those created in ambient air conditions do not support single photon emission. Combining the optical features of the UV-induced defects with density functional theory (DFT) calculations, we attribute the quantum defects generated in vacuum to pristine sulfur vacancies, whereas those in air to oxygen-passivated sulfur vacancies. These findings highlight the feasibility of creating SPEs in TMD monolayers through a scalable, easy-to-implement approach, namely UV illumination in controlled atmosphere. When combined with nowadays sophisticated lighting and optical lithography techniques, <sup>12, 28, 29</sup> photon irradiation is poised to serve as a powerful alternative for controlled SPE creation in TMDs.

#### RESULTS AND DISCUSSION

MoS<sub>2</sub> monolayers used in this study were prepared by mechanical exfoliation of their bulk crystals followed by encapsulation with hBN multilayers, forming hBN/MoS<sub>2</sub>/hBN heterostructures.<sup>30, 31</sup> UV irradiation of the heterostructures was performed at room temperature by placing the samples in a cryostat, which allowed control of the local atmosphere surrounding the heterostructures. All optical measurements were performed at 5 K unless otherwise stated. Fig. 1b shows the optical

spectrum of a representative heterostructure prepared in ambient conditions without UV treatment (Fig. 1a). Two prominent photoluminescence (PL) peaks at 1.95 eV and 1.92 eV, each characteristic of the free neutral excitons ( $X_0$ ) and trions (T),  $^{32}$  respectively, can be observed. To minimize the influence of pre-existing defects in the MoS<sub>2</sub> monolayers, we mainly utilize samples that exhibit negligible defect emission before UV irradiation. Upon UV illumination of the heterostructures in vacuum (Fig. 1c), we observe a transition in the optical properties in certain areas of the samples, and most notably, the emergence of bright, localized emission spots exhibiting sharp PL peaks, as exemplified in Fig. 1d-1f. We refer to these irradiation-induced peaks as  $X_{\text{vacuum}}$ . We observe consistent and reproducible results across multiple samples and numerous bright spots created in vacuum. Most of these  $X_{\text{vacuum}}$  peaks appear at energies of around 1.75 eV, although additional sharp peaks centering at around 1.67 eV and 1.82 eV are also observed (Fig.

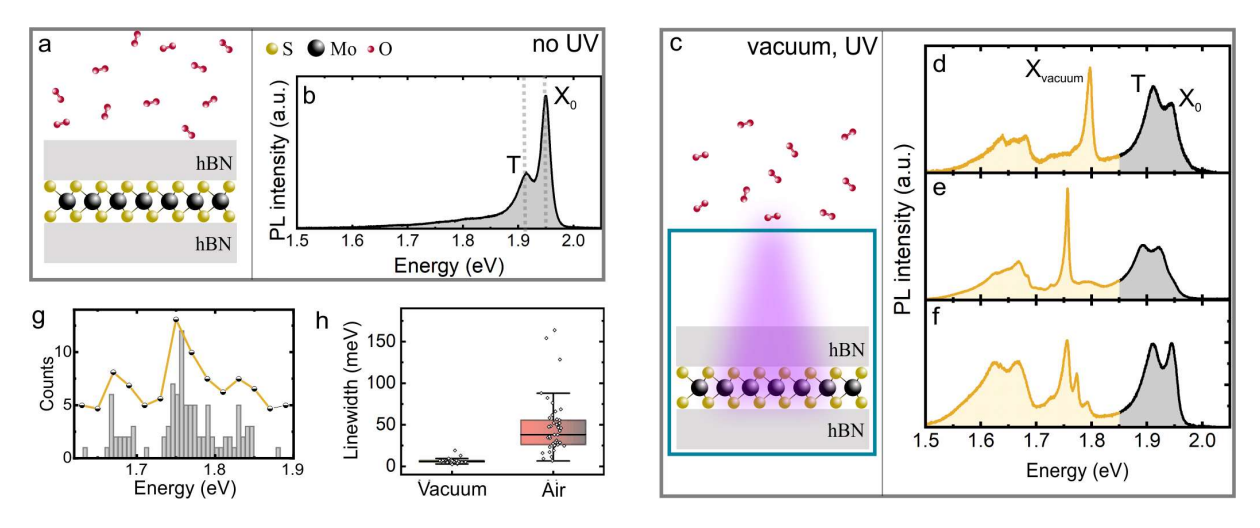


**Figure 1**. (a) Illustration of a hBN/MoS<sub>2</sub>/hBN heterostructure in air. (b) PL spectrum of the heterostructure measured at 5 K. (c) Illustration of a hBN/MoS<sub>2</sub>/hBN heterostructure in vacuum irradiated by UV light. (d – f) Exemplary PL spectra of hBN/MoS<sub>2</sub>/hBN heterostructures irradiated by UV in vacuum. (g) Energy distributions of the  $X_{vacuum}$  peaks created in vacuum. (h) Histograms of PL linewidths of the  $X_{vacuum}$  peaks created in vacuum and the  $X_{air}$  peaks generated in air.

1g). The mean linewidth of the UV-induced  $X_{vacuum}$  peaks is  $6.5 \pm 0.61$  meV, with a minimum value of 2.3 meV (Fig. 1h).

Further careful inspections of the X<sub>vacuum</sub> peaks suggest that they originate from localized midbandgap states. Firstly, they demonstrate PL saturation at high excitation powers. As shown in Fig. 2a and 2b, the PL intensity of the UV irradiation induced sharp X<sub>vacuum</sub> peak at 1.76 eV saturates at high excitation powers (Fig. 2b, yellow), while that of the free excitons and trions still remains linear in this pump power range (Fig. 2b, black). This kind of PL saturation behaviour is commonly observed for localized energy states and is likely associated with ultrafast multi-exciton interactions such as Auger effects in highly confined systems.<sup>22, 33, 34</sup> Secondly, the X<sub>vacuum</sub> peaks possess much longer lifetimes than the delocalized free excitons and trions (Fig. 2c and 2d). By fitting the decay curves of 20 X<sub>vacuum</sub> peaks, each with a double exponential function while deconvoluting the instrument response function, their average lifetime is estimated to be 118  $\pm$ 16.5 ns (Fig. 2f, orange), three orders of magnitude longer compared to the average delocalized free exciton and trion lifetime ( $212 \pm 51.4$  ps, Fig. 2f, black). Such long PL lifetimes have been observed for defects in TMDs, 13, 23 and is again indicative of the localized electronic origins of these UV-induced peaks. Within the effective-mass approximation,<sup>35</sup> the oscillator strength of a (quasi-) two-dimensional exciton can be approximated as the sum of the oscillator strengths of all the unit cells that contribute to the optical transition.<sup>35,36</sup> Compared to the delocalized free excitons and trions, highly confined excitons resulting from localized electronic states possess much smaller oscillator strength, which would lead to longer PL lifetimes compared to the free excitons and trions. Finally, more direct evidence of the quantum confined nature of these irradiation-induced X<sub>vacuum</sub> peaks is provided by the second-order photon correlation measurements. Fig. 2g shows a representative autocorrelation function obtained from a X<sub>vacuum</sub> peak, and the area ratio between

the center peak and the side peaks is estimated to be 0.22. This kind of photon antibunching can be repeatedly observed for various  $X_{vacuum}$  peaks, and their area ratios vary between 0.05 to 0.42, yielding an average value of 0.20  $\pm$  0.07. We believe that the variation in the area ratio is due to

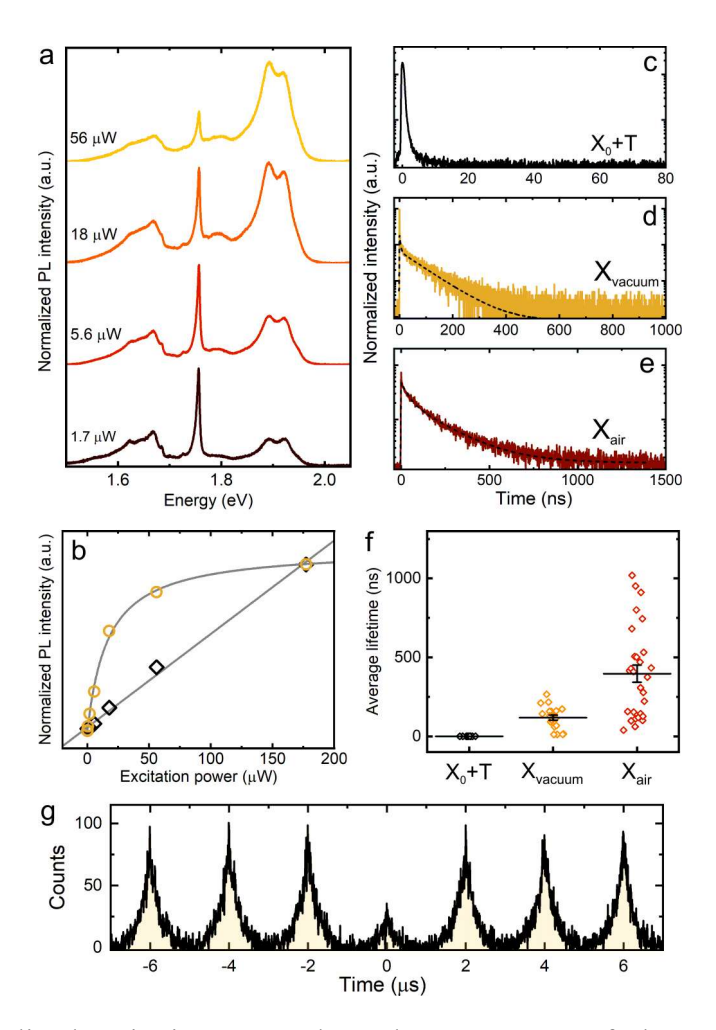


**Figure 2**. (a) Normalized excitation power-dependent PL spectra of a heterostructure irradiated by UV in vacuum. (b) Normalized excitation power-dependent PL intensities of the UV-induced  $X_{\text{vacuum}}$  peak at 1.76 eV (yellow circles) and the free excitons and trions (black diamond) in (a). The gray lines are fits to the data. (c – e) Representative PL decay curves of free excitons ( $X_0$ ) and trions (T) (c), a UV-induced  $X_{\text{vacuum}}$  peak (d), and a UV-induced  $X_{\text{air}}$  peak (e). Dashed lines in (d) and (e) are biexponential fits to the decay curves by deconvoluting the instrument response function. (f) Distributions of the average lifetimes of the free excitons and trions (black),  $X_{\text{vacuum}}$  (yellow) and  $X_{\text{air}}$  (red) peaks. (g) Second-order photon correlation trace of a UV-induced  $X_{\text{vacuum}}$  peak.

contributions from backgrounds. These could include free exciton/trion emission, crosstalk between the two single photon detectors, and laser leakage. The observation of photon antibunching from these new states explicitly suggests their SPE nature.

In light of the SPEs generated upon UV irradiation, we continue to investigate their origins by studying the influence of the irradiation environment. Fig. 3a-3d show an exemplary case of a heterostructure illuminated in air for various amounts of time. Similar to the samples irradiated in vacuum, the originally dim yet uniform PL emission from the heterostructure increases with the UV irradiation time, accompanied by the emergence of bright, localized emission hotspots distributed over the entire monolayer (Fig. 3c and 3d). Yet different from the case of UV irradiation in vacuum, the PL spectra in these notably brighter areas generated in air indicate the introduction of broad PL peaks at around 1.77 eV and 1.70 eV (Fig. 3e, right). We denote these notably broader, UV-induced new peaks in air as  $X_{air}$ , whose average linewidth is determined to be 47.3  $\pm$  1.0 meV, much broader compared to those of the  $X_{vacuum}$  peaks (Fig. 1h).

Aside from the drastically distinct spectral linewidths and emission energies of the  $X_{air}$  and  $X_{vacuum}$  peaks created in the two types of environments, the UV irradiation time required to generate the peaks is also profoundly different. A set of PL spectra of a heterostructure irradiated in air for various amounts of time is shown in Fig. 3f. Care is taken to ensure that the PL spectra were recorded from the same spot on the sample and under similar measurement conditions. The broad  $X_{air}$  peaks start to emerge within one hour's irradiation time and rapidly outcompete the free exciton and trion peaks, becoming the dominant features in the PL spectra. To quantitatively reflect the evolution of the PL spectra with the UV irradiation time, we evaluate the integrated PL intensity ratios ( $I_D/I_0$ ) between the  $X_{air}$  peaks ( $I_D$ ) and the free exciton and trion peaks ( $I_0$ ) as a function of the illumination time, as shown in Fig. 3g (see Fig. S1 for a magnified view). The

intensity ratio increases slowly in the first hour, and then follows increasingly steeper slopes until it reaches a plateau in around a few hours' time. In stark contrast, under similar UV irradiation conditions, it typically takes more than one day's continuous UV irradiation to generate the sharp  $X_{\text{vacuum}}$  peaks (Fig. 3h), suggesting the much larger activation energies required to create the new states in vacuum. It is worth mentioning that the  $X_{\text{vacuum}}$  peaks can still be observed at cryogenic temperatures after the heterostructures are exposed to air, suggesting that the irradiation-induced electronic states remain stable in air. Another drastic contrast between the two types of peaks

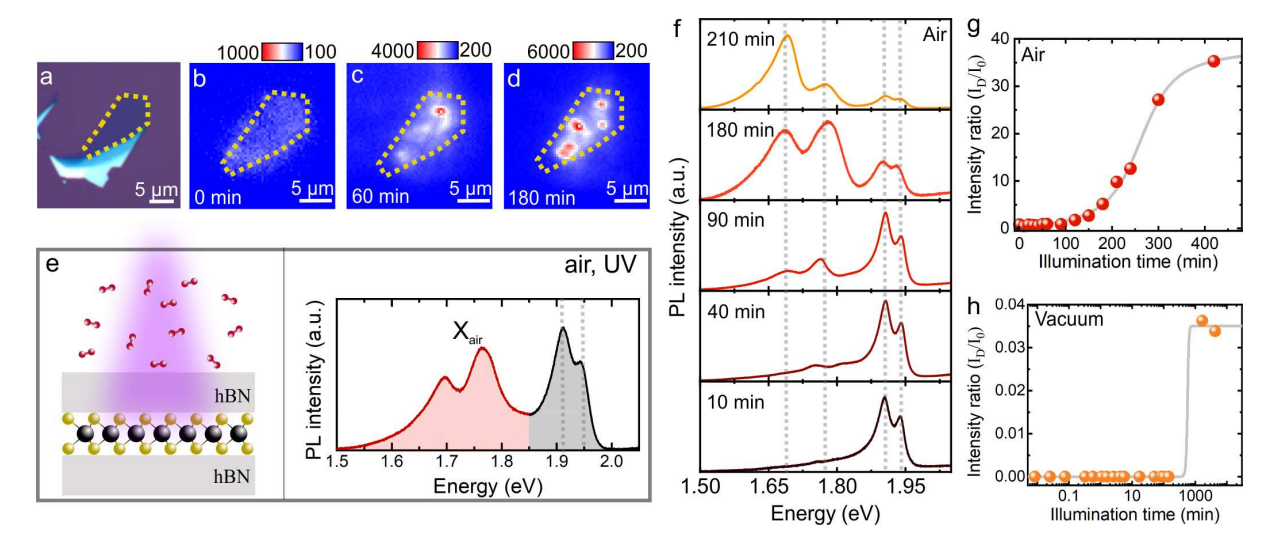


Figure 3. (a) Optical micrograph of a representative  $MoS_2$  monolayer before it is encapsulated by the hBN multilayers. (b - d) PL images of a hBN/MoS<sub>2</sub>/hBN heterostructure after being illuminated by UV in air for various amounts of time. The integration times of the PL images are all 5 s. (e) Illustration of a hBN/MoS<sub>2</sub>/hBN heterostructure in air irradiated by UV (left) and its PL spectrum at 5 K (right). (f) UV irradiation time-dependent PL spectra of a heterostructure in air. The vertical dashed lines indicate the energies of the free excitons, trions, and the irradiation-induced  $X_{air}$  peaks. (g) The integrated PL intensity ratios ( $I_D/I_0$ ) between the  $X_{air}$  peaks ( $I_D$ ) and the free exciton and trion peaks ( $I_D$ ) as a function of the illumination time for a heterostructure irradiated in air. The gray line is a guide to the eye. (h) The integrated PL intensity ratios ( $I_D/I_0$ ) between the  $X_{vaccum}$  peaks ( $I_D$ ) and the free exciton and trion peaks ( $I_D$ ) as a function of the illumination time for a heterostructure irradiated in vacuum. The gray line is a guide to the eye. Note the x-axis is in a logarithmic scale.

suggesting their different origins is revealed by second-order photon correlation measurements, in which the  $X_{air}$  peaks, including those generated in the early stage of illumination, do not exhibit photon antibunching behaviour (Fig. S2) as was observed for the  $X_{vacuum}$  peaks (Fig. 2g).

It is worth mentioning that, despite the many contrasting optical characteristics of the two types of low-energy states generated in vacuum and air, they also exhibit certain shared features. Firstly, the  $X_{air}$  peaks also show PL saturation at high excitation powers (see Fig. S3), similar to the  $X_{vacuum}$  peaks (Fig. 2b). A second shared property observed for both the  $X_{vacuum}$  and  $X_{air}$  peaks is their long exciton lifetimes (Fig. 2d-2f). The average lifetime from the measurements of 28  $X_{air}$  peaks is estimated to be 396  $\pm$  51.6 ns. These shared features of the UV-induced  $X_{vacuum}$  and  $X_{air}$  peaks, namely their PL saturation at high excitation powers and long PL lifetimes, together with their spatially localized emission and red-shifted emission peaks compared to those of the free excitons and trions, attest their localized defect state origins. However, their apparently different emission energies, linewidths, and activation energies, and most notably, their different photon emission statistics, suggest that very different atomic structures and electronic states are likely responsible for these two types of defect peaks.

To determine the atomic structures of the defects giving rise to the  $X_{\text{vacuum}}$  and  $X_{\text{air}}$  peaks, we perform DFT calculations of a variety of the most relevant and abundant defect candidates. <sup>21, 37-41</sup> We consider the possibility of generating molybdenum vacancies using UV irradiation to be relatively low given their much larger formation energies compared to the UV photon energies used in this study ( $\sim 5 \text{ eV}$ ). <sup>21,41</sup> Our calculations show that pristine MoS<sub>2</sub> monolayers have a direct band gap of  $\sim 1.75 \text{ eV}$  at the  $K \to K$ ' transition (see Fig. S4 for details), consistent with previous DFT calculations for similar systems. <sup>26</sup> The slight underestimation compared to the experimental results has been noted before and is expected at this level of theory. <sup>42</sup> Previous studies comparing

DFT with more accurate methods (such as  $G_0W_0$  many-body perturbation theory) have shown that the energy levels of localized defect states are relatively insensitive to the adopted electronic-structure calculation method, but the energy levels of the delocalized band-edge states do show large variations.<sup>43</sup> For ease of comparison and to partially compensate the underestimated bandgaps, we offset the calculated optical transition energies (E) by the bandgap of the pristine MoS<sub>2</sub> monolayer ( $E_{X0}$ ), and we term their energy difference as  $\Delta E = E_{X0} - E$ . Fig. 4b shows the calculated energy shift,  $\Delta E$ , of the various types of pristine sulfur defects (see Supporting Information S5 for details).<sup>41, 44</sup> These sulfur-related defects should represent those generated in vacuum upon UV irradiation due to the negligible influence of oxygen under this condition. We note that the plotted oscillator strength of the optical transitions is normalized to one, so Fig. 4b is indicative of the transition energies rather than the actual transition probabilities.

We offset the energies of the experimentally obtained PL spectra to that of the free neutral excitons as well. Fig. 4a shows a normalized PL spectrum of a monolayer after being illuminated by UV in vacuum. Together shown is a histogram of the  $X_{vacuum}$  peak energies, and they most often occur at  $\Delta E = 0.11$ , 0.19, and 0.27 eV. For each of the experimentally observed major  $\Delta E$  peak, the DFT theory predicts optical transitions in similar energy ranges. The most abundant defect peak emitting at around 1.75 eV (corresponding to  $\Delta E = 0.19$  eV in Fig. 4a) might be associated with point defects such as di-S vacancies ( $V_{2S}$ ) and S adatoms next to S vacancies, while the S vacancies ( $V_{S}$ ) might be responsible for the  $\Delta E = 0.11$  eV defect peaks, agreeing well with those generated by He-ion irradiations<sup>22</sup> (see Fig. S5 and Table S1 for details). However, an accurate association of point defects with the major  $\Delta E$  peaks is challenging given the level of accuracy we can achieve from the DFT calculations. Nevertheless, these comparisons give a reasonable explanation of the possible atomic origins of the defects. To gain a more thorough understanding of the electronic

structures giving rise to the  $X_{vacuum}$  peaks, Fig. 4c presents the band structure and projected density-of-states (PDOS) of a di-S vacancy ( $V_{2S}$ ) with the two S vacancies being adjacent to each other (Fig. 4d). Compared to the band structure of the pristine  $MoS_2$  monolayer (Fig. S4), the  $V_{2S}$  defect

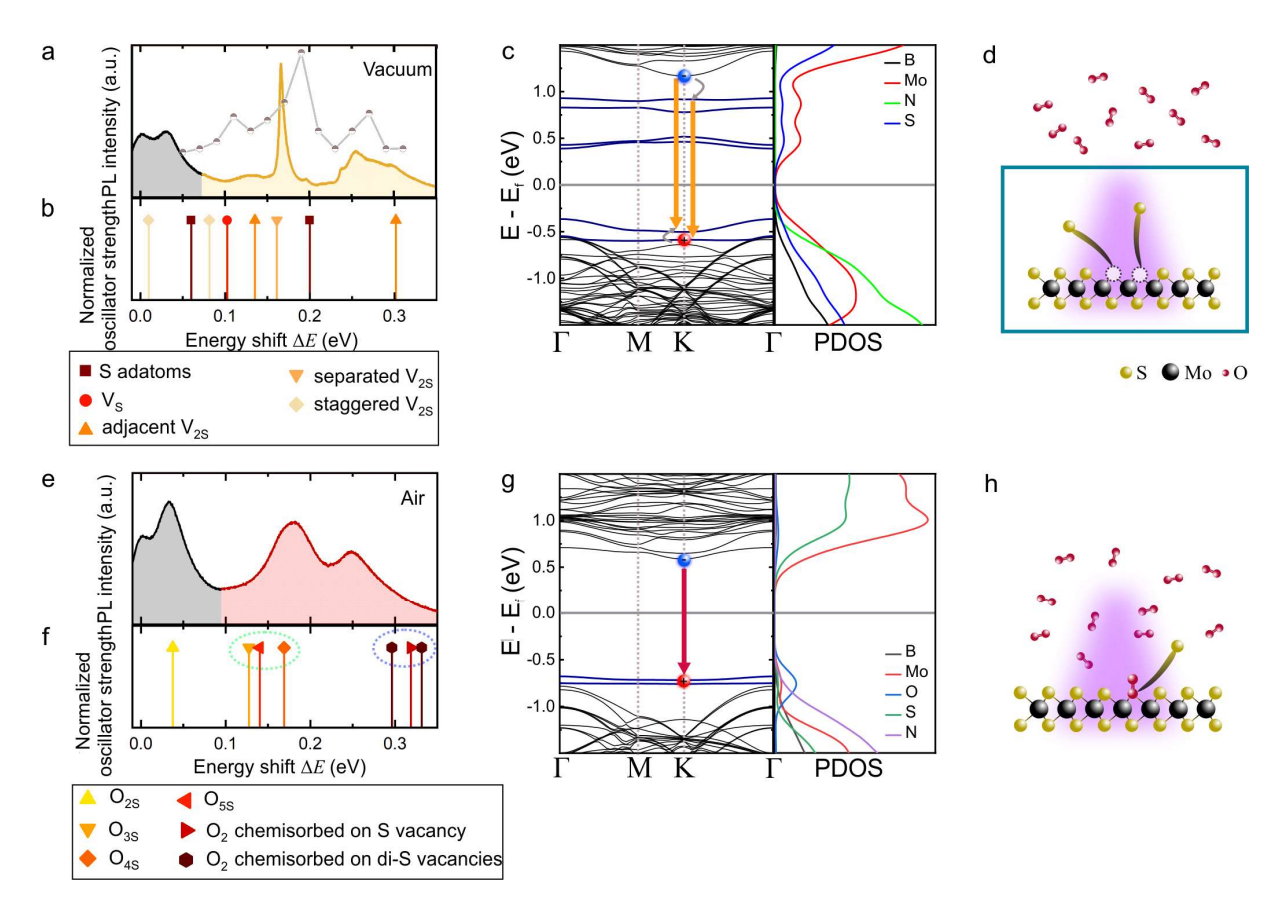


**Figure 4.** (a) PL spectrum of a heterostructure irradiated by UV in vacuum (solid line) and the peak distribution histogram of the irradiation-induced X<sub>vacuum</sub> peaks (circles). Both are offset by the free exciton energy. (b) Calculated optical transition energies of pristine S vacancies. The energies are offset by the bandgaps of the MoS<sub>2</sub> monolayers. (c) Band structure (left) and PDOS (right) of a di-S vacancy (V<sub>2S</sub>) with the two S vacancies being adjacent to each other. (d) Sketch of a UV-irradiation induced di-S vacancy (V<sub>2S</sub>) in vacuum. (e) PL spectrum of a heterostructure irradiated by UV in air. (f) Calculated optical transition energies of oxygen-associated S vacancies. (g) Band structure (left) and PDOS (right) of an O<sub>2</sub> molecule chemisorbed on a S vacancy created by UV irradiation in air. For clarify, the hBN layers are not included in (d) and (h).

introduces a series of highly localized mid-gap states.  $K \to K'$  optical transitions between these defect-induced localized states give rise to the peaks in Fig. 4b (orange upper triangles). We observe similar band structures for the other pristine sulfur defects (Supporting Information S5).

When the MoS<sub>2</sub> monolayers are irradiated in air, consideration of oxygen's presence becomes necessary. Air pockets sandwiched between the stacked multi-layers can be created during the sample preparation stage.<sup>45</sup> Therefore, for the potential atomic defects that could contribute to the X<sub>air</sub> peaks, we mainly consider a variety of commonly observed, oxygen-passivated sulfur defects such as oxygen substituted sulfur vacancies (Os) and O2 molecules chemisorbed on sulfur vacancies, as well as defect clusters.<sup>27,46</sup> Fig. 4e and 4f present the experimental PL spectrum of a MoS<sub>2</sub> monolayer irradiated in air (Fig. 4e) and the simulated optical transitions arising from the various types of oxygen-passivated sulfur vacancies (Fig. 4f), both offset by the free exciton emission energies. Defect structures associated with the higher energy  $X_{air}$  peaks ( $\Delta E = 0.18$  eV) are mostly likely oxygen passivated sulfur vacancy clusters (Fig. 4f green circle, Fig. S6c-6e). These passivated defect clusters can introduce a localized defect state in the valance band, with main contributions from the substituting oxygens. On the other hand, the lower energy  $X_{air}$  peaks  $(\Delta E = 0.25 \text{ eV})$  are likely associated with chemisorbed O<sub>2</sub> molecules on S vacancies (Fig. 4f blue circle, Fig. 4h). O<sub>2</sub> molecules chemisorbed on S vacancies introduce highly localized electronic states to the valence bands, while their conduction bands remain mostly unperturbed (Fig. 4g and Fig. S6f). These assignments are in agreement with previous observations of disappearing broad defect bands when MoS<sub>2</sub> monolayers were subject to in-vacuo high temperature annealing, likely related to the desorption or even dissociation of the oxygen-passivated vacancies. <sup>25, 47</sup>

Taken together, we believe that although both the sharp  $X_{\text{vacuum}}$  peaks created in vacuum and the broad  $X_{\text{air}}$  peaks generated in air originate from S-related defects, the former is primary associated

with pristine, unpassivated S vacancies, whereas the latter have dominating contributions from oxygen-passivated or -decorated S vacancies, consistent with previous observations of defects generated by He-ion irradiaiton.<sup>21, 22</sup> This is also in agreement with the drastically different irradiation time required to generate them: since substitution processes are generally more energetically favourable,<sup>48</sup> it would take much less irradiation time to create the oxygen-passivated S vacancies in air compared to that required for the pristine S vacancies in vacuum.

The very different atomic origins of the two types of PL peaks lead to their distinct optical characteristics. While the existence of a larger variety of defect types in air and the associated inhomogeneous effect may partially explain the much broader linewidths of the X<sub>air</sub> peaks, the vastly different band structures of the defects generated in air and vacuum may also contribute to their very disparate spectral linewidths. Specifically, different from the optical transitions associated with the unpassivated sulfur vacancies (Fig. 4c and S4), where mostly defect-to-defect band transitions are expected, the optical transitions of the oxygen-associated S vacancies happen primarily between the delocalized pristine conduction band and the localized defect band (Fig. 4g and S5). This kind of pristine band-to-defect band transitions have previously been observed for defect-localized excitons in Wse<sub>2</sub> monolayers, <sup>13, 49</sup> which typically leads to rather broad defect emission peaks. We speculate that a similar mechanism is at play for the defects generated in air in this study. The different bands participating in the optical transitions may also explain the observation of single photon emission from the X<sub>vacuum</sub> peaks, where only highly localized defect bands are involved, whereas the lack of photon antibunching from the Xair peaks might be associated with the contributions from the delocalized pristine bands.

#### CONCLUSIONS

In summary, we demonstrate the creation of SPEs in MoS<sub>2</sub> monolayers via UV irradiation in vacuum. In stark contrast, defects generated upon UV irradiation in air lack single photon emission characteristics. Combining the experimentally observed spectral features of the two types of defects with DFT calculations, we infer that those created in vacuum and giving rise to single photon emission are most likely unpassivated sulfur vacancies, while the defects engendered in air can be associated with oxygen passivated or decorated sulfur vacancies. These findings suggest that activation energies provided by UV photons are sufficient for creating sulfur-related defects in MoS<sub>2</sub> monolayers. In conjunction with gas environment control, defects with designated optical properties, particularly those that are suitable for single photon emission, can be selectively created. Compared to defect creation approaches relying on high energy electrons or ions, the relatively low energies of the UV photons would allow the primary creation of chalcogen defects rather than transition metal defects, thus helping preserve the structural integrity of the TMD monolayers and ensuring the homogeneity of the defect types. These findings highlight that UV irradiation may serve as a scalable, easy to implement approach for creating quantum photon sources in TMD monolayers.

## Methods

Preparation of hBN/MoS<sub>2</sub>/hBN heterostructures. To prepare a hBN/MoS<sub>2</sub>/hBN heterostructure, a MoS<sub>2</sub> monolayer and hBN multilayers were first prepared by mechanical exfoliation of their bulk crystals.<sup>30</sup> The top hBN multilayer was then picked up using polydimethylsiloxane (PDMS)/polycarbonate transparent stamps pre-deposited on glass slides.<sup>30, 31</sup> The same procedure

was used to subsequently pick up the MoS<sub>2</sub> monolayer. The stacked hBN/MoS<sub>2</sub> heterostructure was then transferred onto the bottom hBN multilayer. Subsequently, the resultant hBN/MoS<sub>2</sub>/hBN heterostructure was released from the PDMS stamp at 170 °C. Finally, the heterostructure was soaked in chloroform for 20 min to remove the polycarbonate.

UV irradiation of the heterostructures. A UV lamp (SLS204, Thorlabs) with a maximum output power of 0.34 mW at 250 nm was used to irradiate the heterostructures for designated amounts of time at room temperature. Specifically, the as-prepared hBN/MoS<sub>2</sub>/hBN heterostructures were loaded into a liquid He cryostat. For UV irradiation in air, the cryostat was purged with air, and the heterostructures were illuminated by the UV lamp for designated amounts of time. To perform UV irradiation in vacuum, the vacuum level inside the cryostat was kept below 5x10<sup>-6</sup> mbar throughout the irradiation process. To account for the absorption of the UV light by the top hBN encapsulation layers, we measured thicknesses of the top hBN layers using AFM and estimated the absorption percentages of the UV light by the top hBN layers. The irradiation conditions were then calibrated to ensure that similar conditions were used for different samples.

**Low-temperature optical measurements.** The continuous-flow liquid He cryostat with the hBN/MoS<sub>2</sub>/hBN heterostructures irradiated by UV for various amounts of time was loaded onto a home-built confocal laser microscope. To excite the samples, a diode laser with a wavelength of 400 nm was used. The excitation laser beam was focused onto the samples by a microscope objective ( $40\times$ , NA = 0.7). Photoluminescence from the MoS<sub>2</sub> monolayers was collected by the same objective and directed to a spectrograph equipped with a charge-coupled device for imaging and spectroscopic measurements. Time-resolved PL measurements were performed using single-photon avalanche diodes. Photon correlation measurements were performed by splitting the signal

using a beam splitter and focusing them onto two identical single photon avalanche diodes in a Hanbury-Brown and Twiss geometry.

Electronic structure calculations. The structures were optimized with the conjugate gradient (CG) algorithm in the Spanish Initiative for Electronic Simulations with Thousands of Atoms (SIESTA) program (version 4.1 b4),<sup>40, 50</sup> with the generalized gradient approximation (GGA) Perdew Becke and Ernzerhof (PBE) functional and the DZP basis for all atoms. The basis set was of the split-valence type using the default energy cutoffs of 20 Ry. Mesh cutoffs and filter cutoffs of 200 Ry and 150 Ry were used respectively. The energy tolerance was 1.0 e<sup>-5</sup> and the density matrix tolerance was 1.0 e<sup>-5</sup>. Fermi Dirac smearing was applied at an electronic temperature of 300 K. Optimizations were performed using the Gamma centered Monkhorst Pack k grid scheme of 4×4×1 for all cells. Van der Waals interactions were taken into account with the molecular mechanics potentials by Grimme,<sup>51</sup> used as implemented in SIESTA. Band structure calculations were performed using the ReciprocalLatticeVectors option and the same theoretical levels and cutoffs as the optimizations, including the k-grid scheme.

# ASSOCIATED CONTENT

**Supporting Information**. The following files are available free of charge.

PL intensity ratio as a function of the illumination time (PDF)

Photon emission statistics of  $X_{air}$  peaks (PDF)

Pump-power dependent PL spectra of hBN/MoS<sub>2</sub>/hBN heterostructures irradiated in air (PDF)

Electronic structures of pristine MoS<sub>2</sub> monolayers (PDF)

Electronic structures of pristine S-defects in MoS<sub>2</sub> monolayers (PDF)

Electronic structures of oxygen passivated S-defects in MoS<sub>2</sub> monolayers (PDF)

**AUTHOR INFORMATION** 

**Corresponding Author** 

\*Email: <u>xuedanma@anl.gov</u>

Notes

The authors declare no competing final interest.

**ACKNOWLEDGMENT** 

We acknowledge support from the Center for Molecular Quantum Transduction, an Energy

Frontier Research Center funded by the U.S. Department of Energy, Office of Science, Office of

Basic Energy Sciences, under award no. DE-SC0021314 (theoretical calculations). W.W.

acknowledges support from the National Science Foundation DMR Program under award no.

DMR-1905990 (sample preparation). X.M. acknowledges support from the U.S. Department of

Energy, Office of Science, National Quantum Information Science Research Centers for

manuscript preparation. Work performed at the Center for Nanoscale Materials, a U.S. Department

of Energy Office of Science User Facility, was supported by the U.S. DOE, Office of Basic Energy

Sciences, under Contract No. DE-AC02-06CH11357.

REFERENCES

1. Stehr, J.; Buyanova, I.; Chen, W., Defects in advanced electronic materials and Novel low

dimensional structures. Woodhead Publishing: Duxford, United Kingdom, 2018.

18

- 2. Liang, Q.; Zhang, Q.; Zhao, X.; Liu, M.; Wee, A. T. S. Defect Engineering of Two-Dimensional Transition-Metal Dichalcogenides: Applications, Challenges, and Opportunities. *ACS Nano* **2021**, *15*, 2165-2181.
- 3. Zaumseil, J. Luminescent Defects in Single-Walled Carbon Nanotubes for Applications. *Adv. Opt. Mater.* **2021**, 2101576.
- 4. Aharonovich, I.; Englund, D.; Toth, M. Solid-state single-photon emitters. *Nat. Photon.* **2016**, *10*, 631-641.
- 5. Ma, X.; Hartmann, N. F.; Baldwin, J. K. S.; Doorn, S. K.; Htoon, H. Room-temperature single-photon generation from solitary dopants of carbon nanotubes. *Nat. Nanotechnol.* **2015**, *10*, 671-675.
- 6. Xu, R.; Jang, H.; Lee, M.-H.; Amanov, D.; Cho, Y.; Kim, H.; Park, S.; Shin, H.-j.; Ham, D. Vertical MoS2 Double-Layer Memristor with Electrochemical Metallization as an Atomic-Scale Synapse with Switching Thresholds Approaching 100 mV. *Nano Lett.* **2019**, *19*, 2411-2417. 7. Jones, A. M.; Yu, H.; Schaibley, J. R.; Yan, J.; Mandrus, D. G.; Taniguchi, T.; Watanabe, K.;
- Dery, H.; Yao, W.; Xu, X. Excitonic Luminescence Upconversion in A Two-Dimensional Semiconductor. *Nat. Phys.* **2016**, *12*, 323-327.
- 8. Petö, J.; Ollár, T.; Vancsó, P.; Popov, Z. I.; Magda, G. Z.; Dobrik, G.; Hwang, C.; Sorokin, P. B.; Tapasztó, L. Spontaneous Doping of the Basal Plane of MoS2 Single Layers through Oxygen Substitution under Ambient Conditions. *Nat. Chem.* **2018**, *10*, 1246-1251.
- 9. Zhang, J.; Wu, J.; Zou, X.; Hackenberg, K.; Zhou, W.; Chen, W.; Yuan, J.; Keyshar, K.; Gupta, G.; Mohite, A.; Ajayan, P. M.; Lou, J. Discovering Superior Basal Plane Active Two-Dimensional Catalysts for Hydrogen Evolution. *Mater. Today* **2019**, *25*, 28-34.
- 10. Chernikov, A.; Berkelbach, T. C.; Hill, H. M.; Rigosi, A.; Li, Y.; Aslan, O. B.; Reichman, D. R.; Hybertsen, M. S.; Heinz, T. F. Exciton Binding Energy and Nonhydrogenic Rydberg Series in Monolayer WS2. *Phys. Rev. Lett.* **2014**, *113*, 076802.
- 11. Errando-Herranz, C. et al. Resonance Fluorescence from Waveguide-Coupled, Strain-Localized, Two-Dimensional Quantum Emitters. *ACS Photonics* **2021**, *8*, 1069-1076.
- 12. Stanford, M. G.; Rack, P. D.; Jariwala, D. Emerging nanofabrication and quantum confinement techniques for 2D materials beyond graphene. *npj 2D Materials and Applications* **2018**, *2*, 1-15.
- 13. Moody, G.; Tran, K.; Lu, X.; Autry, T.; Fraser, J. M.; Mirin, R. P.; Yang, L.; Li, X.; Silverman, K. L. Microsecond Valley Lifetime of Defect-Bound Excitons in Monolayer WSe2. *Phys. Rev. Lett.* **2018**, *121*, 057403.
- 14. al., Rivera P. et. Intrinsic donor-bound excitons in ultraclean monolayer semiconductors. *Nat. Commun.* **2021**, *12*, 871.
- 15. N. Morell, A. Reserbat-Plantey, I. Tsioutsios, K. G. Schädler, F. Dubin, F. H. L. Koppens, A. Bachtold. High Quality Factor Mechanical Resonators Based on WSe2 Monolayers. *Nano Lett.* **2016**, *16*, 5102-5108.
- 16. H.-K. Li, K. Y. Fong, H. Zhu, Q. Li, S. Wang, S. Yang, Y. Wang, X. Zhang Valley optomechanics in a monolayer semiconductor. *Nat. Photon.* **2019**, *13*, 397-401.
- 17. Branny, A.; Kumar, S.; Proux, R.; Gerardot, B. D. Deterministic strain-induced arrays of quantum emitters in a two-dimensional semiconductor. *Nat. Commun.* **2017**, *8*, 15053.
- 18. Palacios-Berraquero, C.; Kara, D. M.; Montblanch, A. R.-P.; Barbone, M.; Latawiec, P.; Yoon, D.; Ott, A. K.; Loncar, M.; Ferrari, A. C.; Atatüre, M. Large-scale quantum-emitter arrays in atomically thin semiconductors. *Nat. Commun.* **2017**, *8*, 15093.

- 19. Luo, Y.; Shepard, G. D.; Ardelean, J. V.; Rhodes, D. A.; Kim, B.; Barmak, K.; Hone, J. C.; Strauf, S. Deterministic coupling of site-controlled quantum emitters in monolayer WSe2 to plasmonic nanocavities. *Nat. Nanotechnol.* **2018**, *13*, 1137-1142.
- 20. Peng, L.; Chan, H.; Choo, P.; Odom, T. W.; Sankaranarayanan, S. K. R. S.; Ma, X. Creation of Single-Photon Emitters in WSe2 Monolayers Using Nanometer-Sized Gold Tips. *Nano Lett.* **2020**, *20*, 5866-5872.
- 21. Mitterreiter, E.; Schuler, B.; Cochrane, K. A.; Wurstbauer, U.; Weber-Bargioni, A.; Kastl, C.; Holleitner, A. W. Atomistic Positioning of Defects in Helium Ion Treated Single-Layer MoS2. *Nano Lett.* **2020**, *20*, 4437-4444.
- 22. Klien, J. et al. Site-selectively generated photon emitters in monolayer MoS2 via local helium ion irradiation. *Nat. Commun.* **2019**, *10*, 2755.
- 23. Qian, Q.; Peng, L.; Perea-Lopez, N.; Fujisawa, K.; Zhang, K.; Zhang, X.; Choudhury, T. H.; Redwing, J. M.; Terrones, M.; Ma, X.; Huang, S. Defect creation in WSe2 with a microsecond photoluminescence lifetime by focused ion beam irradiation. *Nanoscale* **2019**, *12*, 2047-2056. 24. al., Zheng et. Point Defects and Localized Excitons in 2D WSe2. *ACS Nano* **2019**, *13*, 6050-6059.
- 25. Mitterreiter, E. et al. The role of chalcogen vacancies for atomic defect emission in MoS2. *Nat. Commun.* **2021**, *12*, 3822.
- 26. Liu, D.; Guo, Y.; Fang, L.; Robertson, J. Sulfur vacancies in monolayer MoS2 and its electrical contacts. *Appl. Phys. Lett.* **2013**, *103*, 183113.
- 27. Zhou, W.; Zou, X.; Najmaei, S.; Liu, Z.; Shi, Y.; Kong, J.; Lou, J.; Ajayan, P. M.; Yakobson, B. I.; Idrobo, J.-C. Intrinsic Structural Defects in Monolayer Molybdenum Disulfide. *Nano Lett.* **2013**, *13*, 2615-2622.
- 28. Li, L.; Liu, X.; Pal, S.; Wang, S.; Ober, C. K.; Giannelis, W. P. Extreme ultraviolet resist materials for sub-7 nm patterning. *Chem. Soc. Rev.* **2017**, *46*, 4855-4866.
- 29. Kneissl, M.; Seong, T.-Y.; Han, J.; Amano, H. The emergence and prospects of deep-ultraviolet light-emitting diode technologies. *Nat. Photon.* **2019**, *13*, 233-244.
- 30. Castellanos-Gomez, A.; Buscema, M.; Molenaar, R.; Singh, V.; Janssen, L.; van der Zant, H. S. J.; Steele, G. A. Deterministic transfer of two-dimensional materials by all-dry viscoelastic stamping. *2D Mater.* **2014**, *1*, 011002.
- 31. Zomer, P. J.; Guimarães, M. H. D.; Brant, J. C.; Tombros, N.;van Wees, B. J. Fast pick up technique for high quality heterostructures of bilayer graphene and hexagonal boron nitride. *Appl. Phys. Lett.* **2014**, *105*, 013101.
- 32. Cadiz, F. et al. Excitonic Linewidth Approaching the Homogeneous Limit in MoS2-Based van der Waals Heterostructures. *Phys. Rev. X* **2017**, *7*, 021026.
- 33. Ma, X.; Adamska, L.; Yamaguchi, H.; Yalcin, S. E.; Tretiak, S.; Doorn, S. K., Htoon, H. Electronic Structure and Chemical Nature of Oxygen Dopant States in Carbon Nanotubes. *ACS Nano* **2014**, *8*, 10782-10789.
- 34. Castelletto, S.; Boretti, A. Silicon carbide color centers for quantum applications. *J. Phys. Photon.* **2020**, *2*, 022001.
- 35. Feldmann, J.; Peter, G.; Göbel, E. O.; Dawson, P.; Moore, K.; Foxon, C.; Elliott, R. J. Linewidth dependence of radiative exciton lifetimes in quantum wells. *Phys. Rev. Lett.* **1987**, *59*, 2337-2340.
- 36. Morrow, D. J.; Ma. X. Trapping interlayer excitons in van der Waals heterostructures by potential arrays. *Phys. Rev. B* **2021**, *104*, 195302.

- 37. Liu, H.; Han, N.; Zhao, J. Atomistic insight into the oxidation of monolayer transition metal dichalcogenides: from structures to electronic properties. *RSC Adv.* **2015**, *5*, 17572.
- 38. Akdim, B.; Pachter, R.; Mou, S. Theoretical analysis of the combined effects of sulfur vacancies and analyte adsorption on the electronic properties of singlelayer MoS2. *Nanotechnology* **2016**, *27*, 185701.
- 39. Khan, M. A.; Erementchouk, M.; Hendrickson, J.; Leuenberger, M. N. Electronic and optical properties of vacancy defects in single-layer transition metal dichalcogenides. *Phys. Rev. B* **2017**, *95*, 245435.
- 40. L. O. Jones, M. A. Mosquera, M. A. Ratner, G. C. Schatz. Control of Charge Carriers and Band Structure in 2D Monolayer Molybdenum Disulfide via Covalent Functionalization. *ACS Appl. Mater. Interfaces* **2020**, *12*, 4607-4615.
- 41. Hong, J. et al. Exploring atomic defects in molybdenum disulphide monolayers. *Nat. Commun.* **2015**, *6*, 6293.
- 42. Perdew, J. P. Density functional theory and the band gap problem. *Int. J. Quantum Chem.* **1985,** *28*, 497-523.
- 43. Chen, W.; Pasquarello, A. Correspondence of defect energy levels in hybrid density functional theory and many-body perturbation theory. *Phys. Rev. B* **2013**, *88*, 115104.
- 44. KC, S.; Longo, R. C.; Addou, R.; Wallace, R. M.; Cho, K. . Impact of intrinsic atomic defects on the electronic structure of MoS2 monolayers. *Nanotechnology* **2014**, *25*, 375703.
- 45. Hong, M.; Yang, P.; Zhou, X.; Zhao, S.; Xie, C.; Shi, J.; Zhang, Z.; Fu, Q.; Zhang, Y. Decoupling the Interaction between Wet-Transferred MoS2 and Graphite Substrate by an Interfacial Water Layer. *Adv. Mater. Interfaces* **2018**, *5*, 1800641.
- 46. Tumino, F.; Casari, C. S.; Bassi, A. L.; Tosoni, S. Nature of Point Defects in Single-Layer MoS2 Supported on Au(111). *J. Phys. Chem. C* **2020**, *124*, 12424-12431.
- 47. Venanzi, T.; Arora, H.; Erbe, A.; Pashkin, A.; Winnerl, S.; Helm, M.; Schneider, H. Exciton localization in MoSe2 monolayers induced by adsorbed gas molecules. *Appl. Phys. Lett.* **2019**, *114*, 172106.
- 48. Komsa, H.-P.; Kotakoski, J.; Kurasch, S.; Lehtinen, O.; Kaiser, U.; Krasheninnikov, A. V. Two-Dimensional Transition Metal Dichalcogenides under Electron Irradiation: Defect Production and Doping. *Phys. Rev. Lett.* **2012**, *109*, 035503.
- 49. Hsu, W.-T.; Chen, Y.-L.; Chen, C.-H.; Liu, P.-S.; Hou, T.-H.; Li, L.-J.; Chang, W.-H. Optically initialized robust valley-polarized holes in monolayer WSe2. *Nat. Commun.* **2015**, *6*, 8963.
- 50. Soler, J. M.; Artacho, E.; Gale, J. D.; García, A.; Junquera, J.; Ordejón, P.; Sánchez-Portal, D. The SIESTA Method for Ab Initio Order-N Materials Simulation. *J. Phys.: Condens. Matter.* **2002,** *14*, 2745-2779.
- 51. Grimme, S. Semiempirical GGA-Type Density Functional Constructed with a Long-Range Dispersion Correction. *J. Comput. Chem.* **2006**, *27*, 1787-1799.

